Myosin IIA drives membrane bleb retraction

Nilay Taneja and Dylan T. Burnette*
Department of Cell and Developmental Biology, Vanderbilt University School of Medicine, Nashville, TN 37232

ABSTRACT **Membrane blebs are specialized cellular protrusions that play diverse roles in processes such as cell division and cell migration. Blebbing can be divided into three distinct phases: bleb nucleation, bleb growth, and bleb retraction. Following nucleation and bleb growth, the actin cortex, comprising actin, cross-linking proteins, and nonmuscle myosin II (MII), begins to reassemble on the membrane. MII then drives the final phase, bleb retraction, which results in reintegration of the bleb into the cellular cortex. There are three MII paralogues with distinct biophysical properties expressed in mammalian cells: MIIA, MIIB, and MIIC. Here we show that MIIA specifically drives bleb retraction during cytokinesis. The motor domain and regulation of the nonhelical tailpiece of MIIA both contribute to its ability to drive bleb retraction. These experiments have also revealed a relationship between faster turnover of MIIA at the cortex and its ability to drive bleb retraction.**

Monitoring Editor
Manuel Théry
CEA, Hopital Saint Louis

Received: Nov 30, 2018
Revised: Feb 6, 2019
Accepted: Feb 13, 2019

INTRODUCTION

The actin cortex is a thin network of actin filaments underneath the plasma membrane that allows a cell to maintain and change shape in response to internal and external stimuli (Salbreux *et al.*, 2012; Fritzsche *et al.*, 2016; Sezgin *et al.*, 2017). Membrane blebs are created upon a local detachment of the cortex from the membrane, which leads to an influx of cytosol, thus creating a spherical protrusion of the membrane (Salbreux *et al.*, 2012). These specialized protrusions play multiple roles, such as releasing cytoplasmic pressure at the polar cortex during cytokinesis, as well as driving pressure-driven cell migration (Sedzinski *et al.*, 2011; Bergert *et al.*, 2015). As such, the mechanisms driving bleb growth and retraction remain active areas of interest.

The newly formed membrane bleb lacks the majority of cortical components. New cortex assembly occurs on this membrane, with ezrin appearing nearly instantaneously, followed by actin appearing ~2 s after bleb formation, and with nonmuscle myosin II (MII) following ~8 s later (Charras *et al.*, 2006). Ezrin was recently shown to recruit MYOGEF to the bleb, which activates RhoA signaling (Jiao *et al.*, 2018). This results in recruitment and activation of MII, which then drives retraction of the bleb. Previous work has suggested that turnover of actin, MII, and actin cross-linkers is critical for bleb retraction (Fritzsche *et al.*, 2013). Specifically, the MII regulatory light chain was shown to turn over at rates intermediate between actin and actin cross-linking protein alpha actinin (Fritzsche *et al.*, 2013). It was proposed that this allows myosin II to reorganize actin network architecture, even in the presence of passive cross-links (Fritzsche *et al.*, 2013). Because the regulatory light chain binds multiple MII paralogues, the specific paralogue responsible for bleb retraction is unknown. Furthermore, the relationship between turnover of that specific paralogue and its correlation with bleb retraction has not been established.

There are three MII paralogues, MIIA, MIIB, and MIIC, with mammalian cells commonly expressing MIIA and MIIB (Vicente-Manzanares *et al.*, 2009). Distinctive roles for MII paralogues have been proposed in multiple contexts, such as stress fiber formation in migrating cells (Beach *et al.*, 2017), cell–cell junction formation in epithelial cells (Smutny *et al.*, 2010), growth cone advance in neurons (Brown and Bridgman, 2003), and proplatelet formation in mice (Lordier *et al.*, 2008; Bluteau *et al.*, 2012). Here we show evidence for MIIA in specifically driving bleb retraction during cytokinesis. We further show that both motor activity at the N-terminus and regulation of the nonhelical tailpiece at the C-terminus control this activity. These experiments have also revealed a correlation between the rate of MII turnover and bleb retraction.

This article was published online ahead of print in MBoC in Press (http://www.molbiolcell.org/cgi/doi/10.1091/mbc.E18-11-0752) on February 20, 2019.

The authors declare no competing financial interest.

N.T. and D.T.B. conceived the study, designed the experiments, and wrote the manuscript. N.T. performed the experiments and analyzed the data.

*Address correspondence to: Dylan T. Burnette (dylan.burnette@vanderbilt.edu).

Abbreviations used: CRISPR, clustered regularly interspaced short palindromic repeats; DIC, differential interference contrast; FRAP, fluorescence recovery after photobleaching; KO, knockout; MII, myosin II; MIIA, myosin IIA; MIIB, myosin IIB; MIIC, myosin IIC; Scr, scrambled siRNA; UT, untransfected.

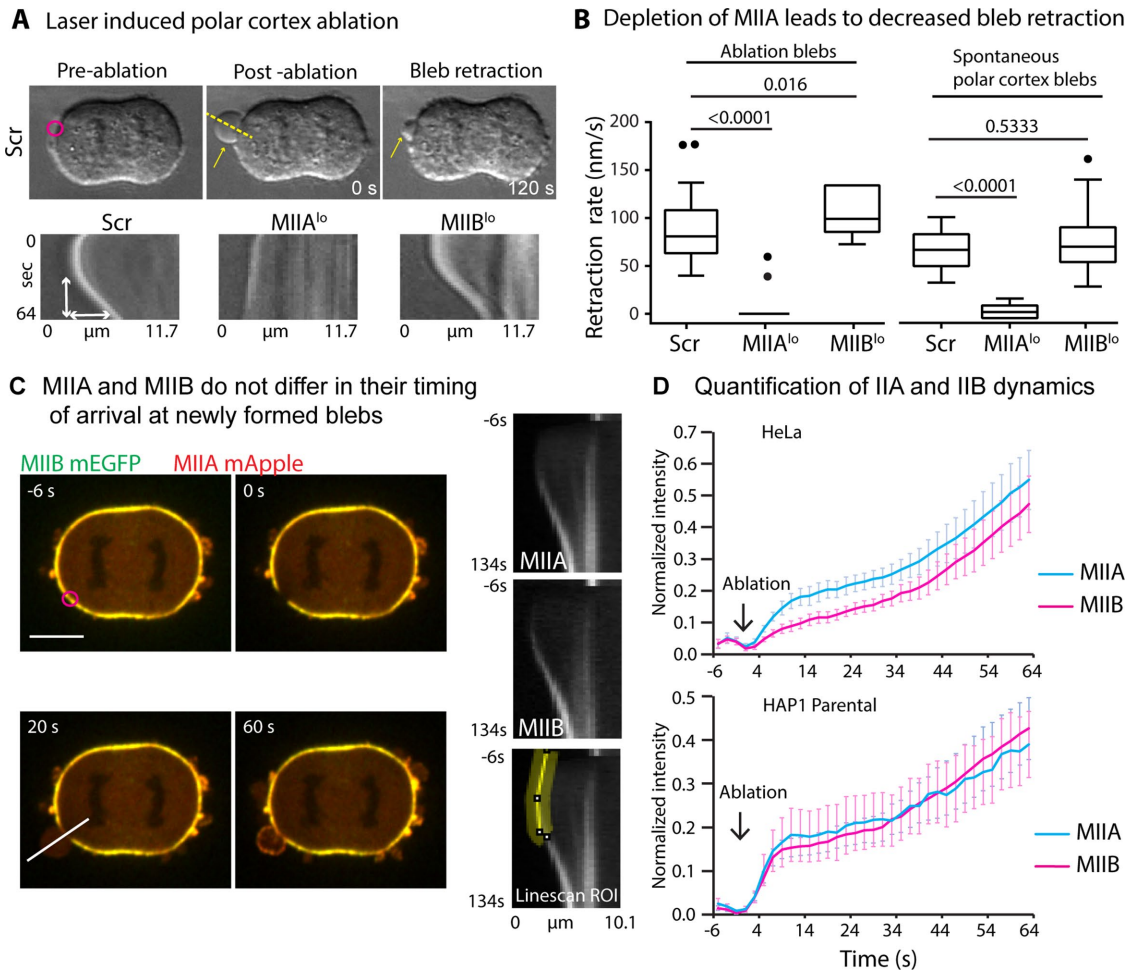

FIGURE 1: MIIA but not MIIB is necessary for bleb retraction. (A) Laser-induced polar cortex ablation in control, MIIA- or MIIB-depleted HeLa cells. Representative control DIC montage shows the ablation ROI (magenta circle) used to create a membrane bleb (yellow arrow). Dotted yellow line represents ROI used to create kymographs. Representative kymographs for each condition are shown below. White arrows show the measurement method for calculating retraction rates. (B) Tukey plots comparing bleb retraction rates for controlled and spontaneous blebs in control vs. MIIA^{lo} or MIIB^{lo} cells. Controlled blebs: $n = 25$ control, 15 MIIA^{lo} and 25 MIIB^{lo} cells from three independent experiments. Spontaneous blebs: $n = 18$ control blebs from 9 cells, 15 MIIA^{lo} blebs from 10 cells, 15 MIIB^{lo} blebs from 10 cells over three independent experiments. (C) Representative time montage of HeLa cell coexpressing MIIA mApple and MIIB mEmerald showing the ablation ROI (magenta circle). Representative kymographs created using the solid white line show MIIA and MIIB recruitment to the bleb. Yellow ROI shows the region of the kymograph compared for recruitment (first 60 s). (D) Comparison of IIA and IIB recruitment to blebs in HeLa and HAP1 fibroblasts. $n = 10$ cells for each cell line over three independent experiments. Exact p values stated over respective bars. Solid black circles represent outliers. Scale bar: 10 µm.

RESULTS AND DISCUSSION

To create a bleb in a controlled manner, we utilized laser ablation as previously described (Tinevez *et al.*, 2009; Sedzinski *et al.*, 2011; Goudarzi *et al.*, 2012). Ablation of the polar cortex in a control cell undergoing cytokinesis resulted in the formation of a bleb followed by retraction over a time period of ~2 min as previously reported (Figure 1A; Charras *et al.*, 2008). We depleted either MIIA or MIIB in HeLa cells, which express only these two paralogues (Supplemental Figure S1) and created blebs. We found that knockdown of MIIA resulted in failure of bleb retraction, whereas MIIB knockdown did not (Figure 1, A and B). We observed a similar trend in spontaneously occurring blebs at the polar cortex (Figure 1B). The lack of an effect on bleb retraction upon MIIB knockdown could result from an inability of MIIB to get recruited to the bleb. To test this, we monitored MIIA and MIIB recruitment to newly formed blebs in live cells coexpressing MIIA mApple and MIIB mEGFP (Figure 1C). We found that both paralogues were recruited to blebs after their formation (Figure 1, C and D). This was also observed in HAP1 fibroblasts (Figure 1D). Given that both MII paralogues are recruited to blebs, other mechanisms likely drive the differences we observed in bleb retraction upon knockdown.

We next wanted to confirm that MIIA was required to drive bleb retraction. To that end, we used a *myh9* (MIIA) knockout HAP1 cell line we previously generated using CRISPR (Fenix *et al.*, 2016), which expresses only MIIB (Supplemental Figure S1). We compared bleb retraction rates in this cell line versus the parental HAP1 cells. Knockout of MIIA resulted in failure of bleb retraction in HAP1 *myh9* KO cells (Figure 2, A and B). Expression of full-length MIIA at 72.6 ± 33% of parental levels restored bleb retraction rates comparable to the parental cell line (Figure 2, B and C, and

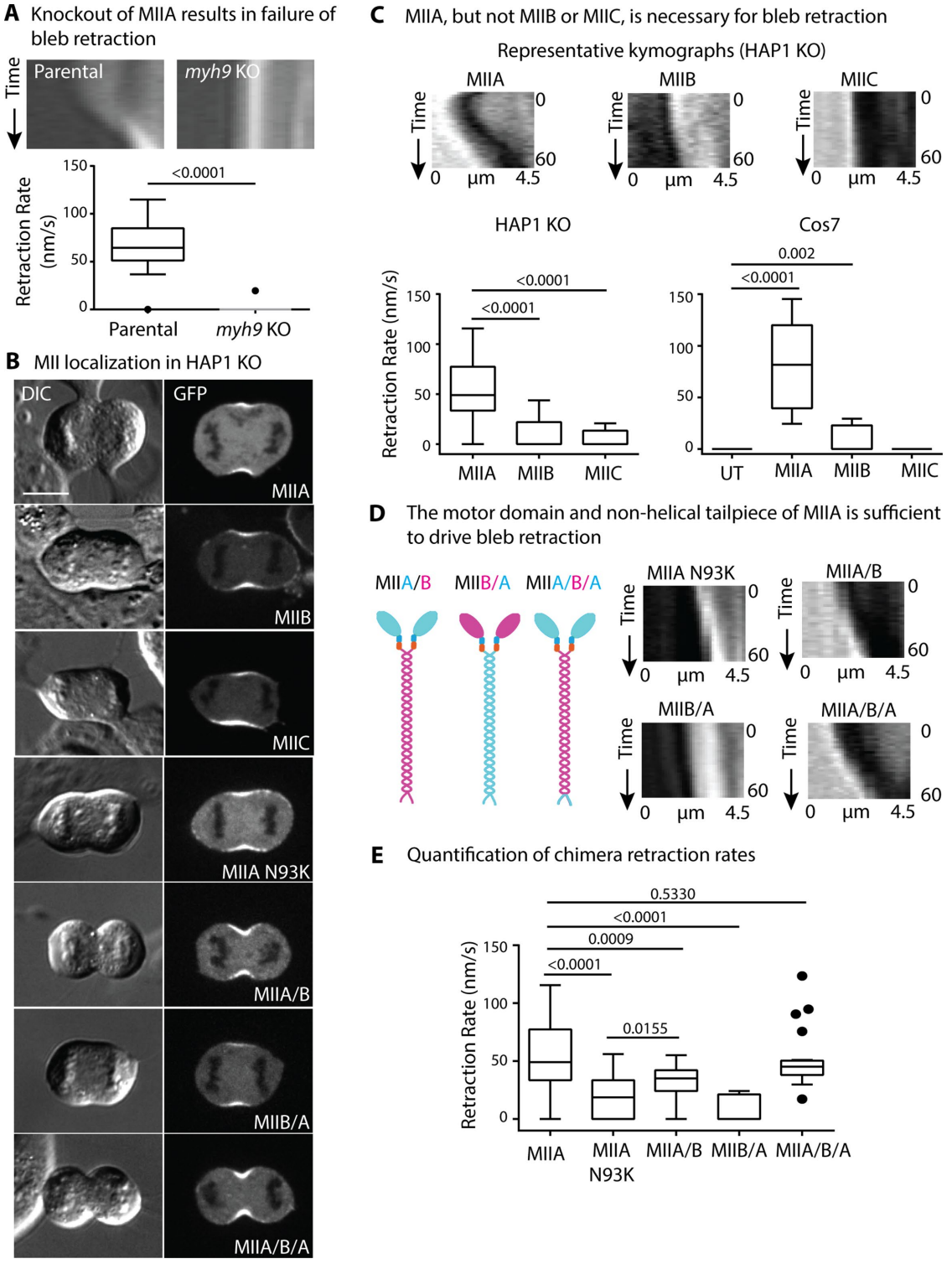

FIGURE 2: The motor domain and nonhelical tailpiece of MIIA are sufficient to drive bleb retraction. (A) Representative kymographs from HAP1 parental and *myh9* KO cells following cortex ablation. $n = 21$ parental cells and 12 KO cells over three independent experiments. (B) Representative DIC and fluorescence images showing the localization of MII paralogues and mutants in HAP1 KO cells. (C) Representative kymographs from MIIA, MIIB, and MIIC expressing HAP1 KO cells following cortex ablation, as in Figure 1. Tukey plots comparing retraction rates in HAP1 KO cells expressing MIIA, MIIB, or MIIC, and Cos7 cells expressing MIIA, MIIB, MIIC, or untransfected (UT). For HAP1 KO cells, $n = 27$ MIIA, 10 MIIB, and 15 MIIC expressing cells over more than three independent experiments. For Cos7 cells, $n = 16$ untransfected, 16 MIIA, 11 MIIB, and 10 MIIC expressing cells over three independent experiments. (D) Representative kymographs showing MIIA N93K, MIIA/B, MIIB/A, and MIIA/B/A expressing HAP1 KO cells following cortex ablation. (E) Retraction rates comparing mutants shown in D. $n = 21$ N93K, 18 MIIA/B, 8 MIIB/A, and 21 MIIA/B/A expressing cells over more than three independent experiments. MIIA bar is from the same data set as C and is displayed only for comparison. Exact *p* values stated over respective bars. Solid circles in Tukey plots represent outliers. Scale bar: 10 µm.

Supplemental Table S1). Similar levels of MIIB or MIIC expression did not rescue bleb retraction (Figure 2, B and C, and Supplemental Table S1). We next wanted to further test the potential roles of MIIB and MIIC in driving bleb retraction. Therefore, we turned to Cos7 cells, which express only MIIB and MIIC (Even-Ram *et al.*, 2007). While cortex ablation resulted in bleb formation, wild-type Cos7 cells failed to retract these blebs (Figure 2C, UT bar). Overexpression of either MIIB or MIIC did not result in bleb retraction (Figure 2C). However, Cos7 cells expressing exogenous MIIA did retract their blebs (Figure 2C). Taken together, our data show that MIIA is required to drive bleb retraction.

MIIA and MIIB primarily differ in their N-terminal motor domain as well as in their C-terminal nonhelical tailpiece (Vicente-Manzanares *et al.*, 2009). We first hypothesized that motor activity of MIIA could play a role in bleb retraction. To test this, we expressed MIIA containing a N93K mutation in the motor domain, which results in reduced ATPase activity of MIIA (Figure 2B; Hu *et al.*, 2002). Expression of MIIA N93K in HAP1 *myh9* KO cells resulted in significantly slower bleb retraction, suggesting the motor domain of MIIA plays a role in bleb retraction (Figure 2, D and E). To test whether the motor domain of MIIA is sufficient to drive bleb retraction, we used chimeric motors, where the motor domains of the MIIA and MIIB were swapped (see schematics, Figure 2D; Vicente-Manzanares *et al.*, 2008). Expression of MIIB/A, bearing the motor domain of MIIB, and the helical rod and nonhelical tailpiece of MIIA, did not rescue bleb retraction (Figure 2, D and E). On the other hand, expression of MIIA/B, bearing the motor domain of MIIA, and the helical rod and nonhelical tailpiece of MIIB significantly rescued bleb retraction (Figure 2, D and E). Interestingly, the MIIA/B chimera did not rescue bleb retraction rates to the same extent as full-length MIIA ($p = 0.0009$). This suggests that in addition to the motor domain of MIIA, other factors also contribute to drive bleb retraction.

Because MIIA and MIIB also differ in their nonhelical tailpiece, we hypothesized that the tailpiece of MIIA may also contribute to bleb retraction. Therefore, we created a chimeric motor, bearing the motor domain and nonhelical tailpiece of MIIA, and the helical rod domain of MIIB (MIIA/B/A). Expression of this construct at levels similar to MIIA/B (55 ± 21% for MIIA/B/A vs. 48 ± 10% for MIIA/B) resulted in statistically indistinguishable rates of bleb retraction compared with full-length MIIA (Figure 2, D and E). Taken together, these data show that the motor domain and nonhelical tailpiece of MIIA, with the rod domain of either MIIA or MIIB, are sufficient to drive bleb retraction.

Current models of bleb retraction propose that myosin II turnover plays a critical role in bleb retraction (Charras *et al.*, 2008; Fritzsche *et al.*, 2013). We therefore measured the turnover of MIIA and MIIB at the cortex using fluorescence recovery after photobleaching (FRAP), as previously performed for the regulatory light chain (Figure 3A; Fritzsche *et al.*, 2013). In HeLa cells, we found that MIIA recovered twice as fast as MIIB (Figure 3B). We confirmed this finding in HAP1 *myh9* KO cells expressing full-length MIIA or MIIB (Figure 3, C and E). Interestingly, MIIC turned over markedly more slowly than MIIA and MIIB in HAP1 *myh9* KO cells (Figure 3, D and E). Similar trends were observed in Cos7 cells (Figure 3F). Taken together, these data suggest that the relatively fast turnover of MIIA correlates with its ability to drive bleb retraction.

To further test whether changes in bleb retraction correlated with changes in turnover of MIIA at the cortex, we measured the turnover of the MIIA mutants and chimeras in HAP1 KO cells. MIIA N93K showed a slower recovery than full-length MIIA, indicating that lower motor activity correlates with slower turnover (Figure 4, A and B). Interestingly, the MIIA/B chimera recovered significantly more slowly than MIIA, but not MIIB (Figure 4, B and C). This suggests that the nonhelical tailpiece of MIIA plays a role in turnover, and its absence in the MIIA/B chimera results in its slower turnover compared with full-length MIIA. To test this, we expressed the MIIA/B/A chimera, comprising the motor domain and nonhelical tailpiece of MIIA and the helical rod domain of MIIB. The MIIA/B/A chimera rescued turnover rates to levels comparable to full-length MIIA, in agreement with our observation that this chimera also rescued bleb retraction rates (Figure 4, B and C). Taken together, these data suggest that both the motor domain and the nonhelical tailpiece of MIIA contribute to its fast turnover relative to MIIB or MIIC. We next wanted to determine the basis for regulation of MIIA turnover by the nonhelical tailpiece.

Previous studies have proposed phosphorylation of the myosin heavy chain at the nonhelical tailpiece results in MIIA filament disassembly during interphase (Dulyaninova *et al.*, 2007; Dulyaninova and Bresnick, 2013; Breckenridge *et al.*, 2008). To test whether phosphorylation of the nonhelical tailpiece regulates MIIA turnover at the polar cortex during cytokinesis, we expressed an MIIA mutant lacking the nonhelical tailpiece (Figure 5A). Deletion of the nonhelical tailpiece significantly slowed MIIA turnover (Figure 5B). The nonhelical tailpiece contains a single phosphorylation site that could regulate turnover (Ser 1943). We therefore created a phospho-null mutant of MIIA at this site (S1943A) and measured turnover using FRAP. We found that MIIA S1943A also recovered more slowly than wild-type MIIA (Figure 5B). Given the slower turnover of these MIIA tail mutants, we hypothesized that bleb retraction should be slower in these mutants. Indeed, both the MIIA Δtailpiece and MIIA S1943A mutants showed significantly slower bleb retraction (Figure 5, C and D).

Finally, we wanted to test the distinct role of MIIA in driving bleb retraction during interphase. To that end, we used filamin-deficient M2 cells that constitutively bleb during interphase, a classic model system used to study membrane blebbing (Figure 5E; Charras *et al.*, 2006; Bovellan *et al.*, 2014). We probed the expression of the three MII paralogues in M2 cells, and found they express all three paralogues (Supplemental Figure S1). To test their potential roles, we depleted each of the MII paralogues using small interfering RNA (siRNA) knockdown, and measured bleb retraction rates. Knockdown of MIIA, but not MIIB or MIIC, significantly impaired bleb retraction, suggesting that MIIA is the paralogue that drives bleb retraction even during interphase (Figure 5, F and G).

Here we show that MIIA is the specific paralogue that is necessary and sufficient to drive bleb retraction during interphase and cytokinesis. We confirmed this finding using three independent approaches: knocking down MIIA, knocking out MIIA, and expressing IIA in a cell line that does not normally express it. We also showed that the motor domain and the nonhelical tailpiece both regulate bleb retraction. The motor domain of MIIA has distinct biophysical properties compared with MIIB and MIIC, namely, having higher ATPase activity, as well as spending a smaller proportion of its mechanochemical cycle bound to actin in the force-generating state (i.e., lower duty ratio; Kovács *et al.*, 2003; Wang *et al.*, 2003). Interestingly, we found these biophysical properties correlated with faster turnover at the cortex compared with MIIB and MIIC.

Reducing MIIA's motor activity using the N93K mutation slowed the turnover of MIIA at the cortex, which correlated with slower bleb retraction. Replacing the motor domain of MIIA with the motor domain of MIIB also slowed turnover ($p = 0.0257$); this construct also did not support bleb retraction. These findings thus establish a link between the turnover rate and motor activity of MIIA. The positive correlation between MIIA turnover and bleb retraction supports previous experimental and theoretical studies suggesting that

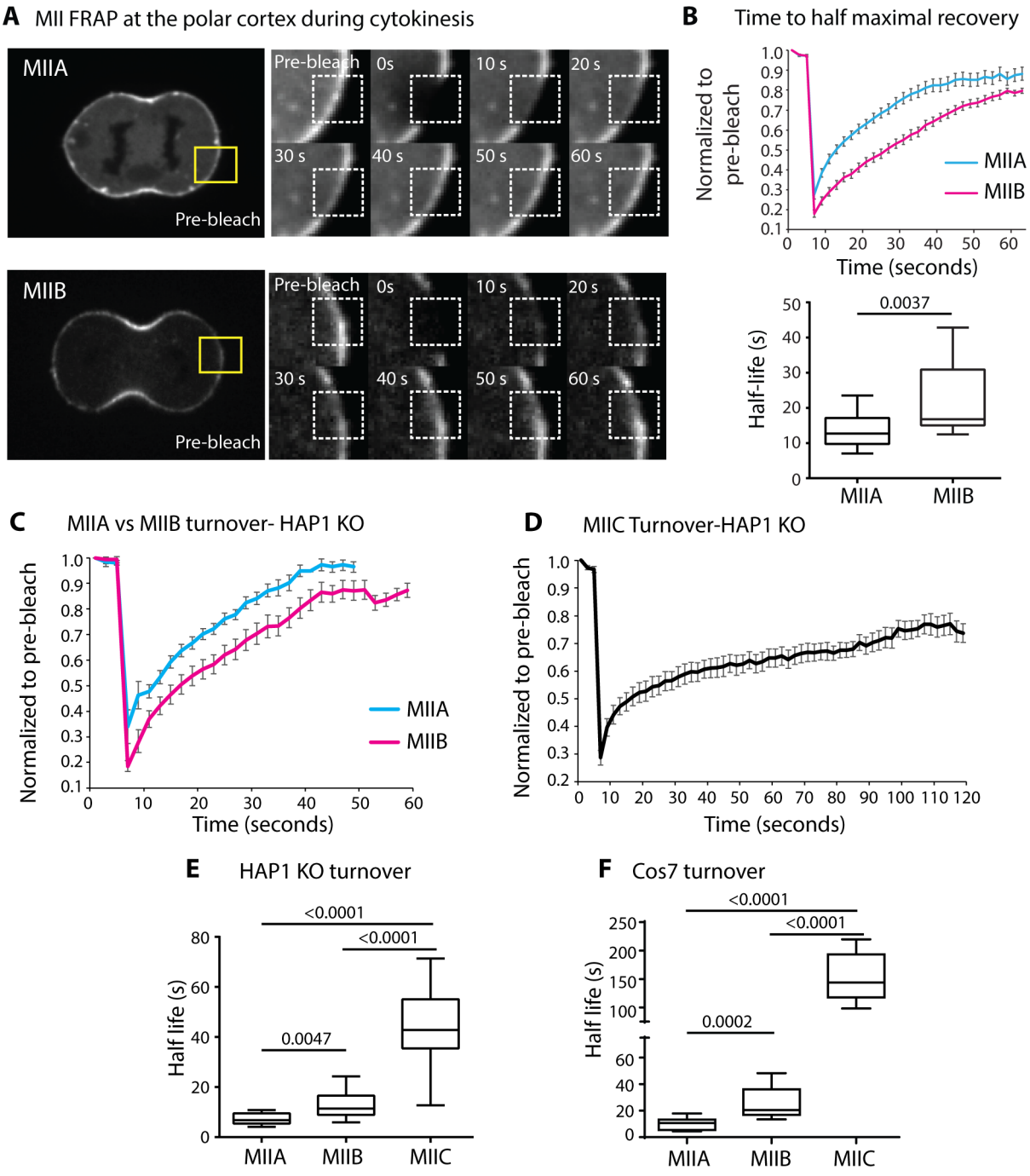

FIGURE 3: MIIA shows fast turnover compared with MIIB and MIIC at the cortex. (A) Representative time montages from two separate cells showing FRAP of MIIA and MIIB mEGFP expressed in HeLa cells. Inset shows an enlarged view of the yellow box. Dotted white box represents the bleaching region. (B) Averaged FRAP curves for MIIA and MIIB in HeLa cells. $n = 15$ cells each for MIIA and MIIB over three independent experiments. See *Materials and Methods* for the curve fitting method. (C, D) Averaged FRAP curves for MIIA and MIB mEGFP (C), and MIIC mEGFP (D) expressed in HAP1 KO cells. (E) Tukey plots showing time for half-maximal recovery for MIIA, MIIB, and MIIC in HAP1 KO cells. $n = 11$ MIIA, 13 MIIB, and 11 MIIC expressing cells over three independent experiments. (F) Tukey plots showing time for half-maximal recovery for MIIA, MIIB, and MIIC in Cos7 cells. $n = 11$ MIIA, 9 MIIB, and 10 MIIC expressing cells over three independent experiments. Exact p values stated over respective bars.

turnover is critical for bleb retraction (Charras *et al.*, 2008; Fritzsche *et al.*, 2013). A limitation of our current study, as well as previous studies that have measured MII turnover, is that we correlated measurements made at the cortex with bleb retraction rates (Fritzsche *et al.*, 2013). We were unable to combine photoablation to create a bleb and photobleaching to measure MII turnover within the same bleb.

We further showed that the nonhelical tailpiece of MIIA also regulates its turnover. Deletion of this segment resulted in both slower turnover and slower bleb retraction. Of note, this effect was

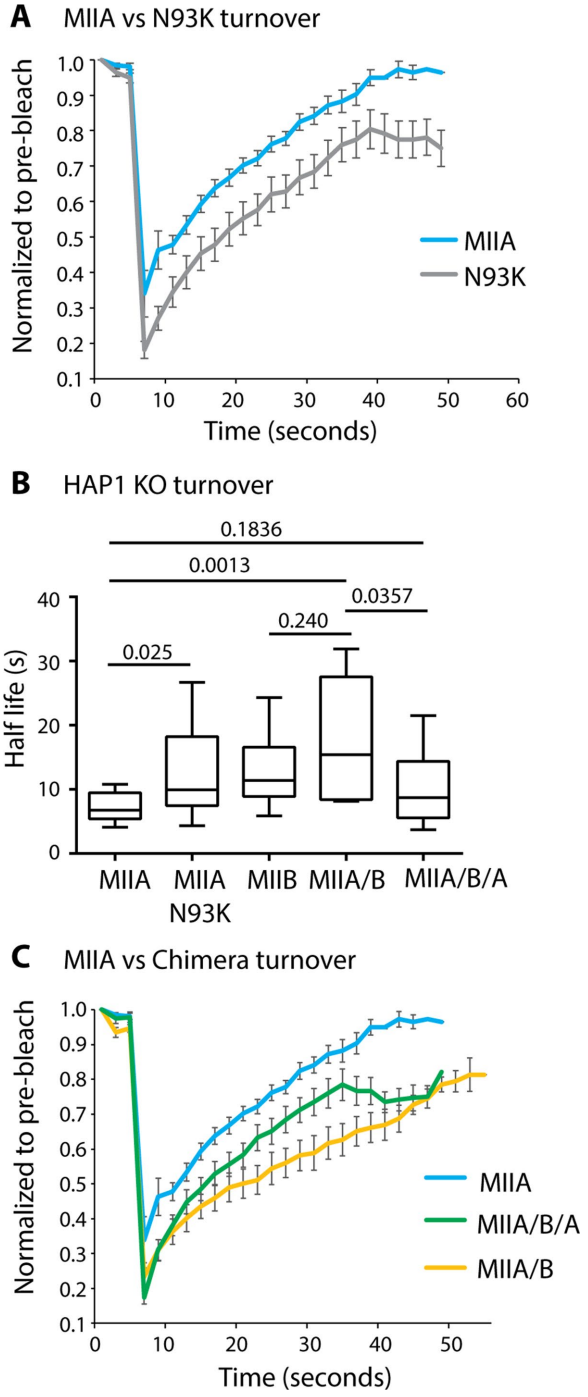

FIGURE 4: The motor domain and nonhelical piece of MIIA both contribute to turnover at the cortex. (A) Averaged FRAP curves for full-length MIIA (from Figure 3C) and MIIA N93K mutant. (B) Tukey plots comparing time for half-maximal recovery for MIIA, MIIA N93K, MIIA/B, MIIB, and MIIA/B/A in HAP1 KO cells. $n = 12$ N93K, 10 MIIA/B, and 13 MIIA/B/A expressing cells over three independent experiments. The MIIA and MIIB data sets are the same as Figure 3C and are only shown for comparison. (C) Averaged FRAP curves for MIIA (from Figure 3C), MIIA/B, and MIIA/B/A chimera. Exact *p* values stated over respective bars.

not specific to MIIA, because deletion of the nonhelical tailpiece of MIIB also resulted in slower turnover of MIIB (Supplemental Figure S2). Not surprisingly, this did not change MIIB's inability to drive bleb retraction (Supplemental Figure S2). While the motor domain of MIIA is absolutely required for bleb retraction, the nonhelical tailpiece may add an additional layer of regulation. This finding is in agreement with previous studies that have proposed that heavy chain phosphorylation controls MIIA disassembly from filaments (Dulyaninova *et al.*, 2007; Dulyaninova and Bresnick, 2013; Breckenridge *et al.*, 2008). Our finding that Ser1943 regulates bleb retraction also suggests an important role for casein kinase II in regulating MIIA heavy chain phosphorylation, which has been shown to phosphorylate Ser1943 in vitro (Kelley and Adelstein, 1990; Dulyaninova *et al.*, 2005). The development of biosensors as well as specific, fast acting inhibitors will likely be necessary to better understand the mechanisms regulating MIIA assembly state during the cell cycle and at the polar cortex.

Membrane blebs play diverse roles in cellular physiology. During cytokinesis, blebs serve as pressure release valves to regulate intracellular pressure and when deregulated, result in dramatic cell shape instabilities and cytokinetic failure (Sedzinski *et al.*, 2011). We have established that MIIA is the major paralogue that drives bleb retraction during cytokinesis. Therefore, a high level of MIIA expression may amplify genome instability through deregulation of cell shape during cytokinesis in cancer cells. Although we did not find a role for MIIB or MIIC in bleb retraction, it is still possible that they may have other roles at the cortex during cytokinesis. The slower turnover of MIIB and MIIC, combined with their lower ATPase activity may make these paralogues better suited to act as cross-linkers at the cellular cortex, thus maintaining cortex stability. Cells also employ blebbing as a mode of migration, both during development and cancer progression (Trinkaus, 1973; Kageyama, 1977; Friedl and Wolf, 2003; Sahai and Marshall, 2003; Blaser *et al.*, 2006). Interestingly, certain types of cancers up- or down-regulate MII paralogues (Maeda *et al.*, 2008; Derycke *et al.*, 2011). Our finding that MII paralogues have distinct roles in bleb retraction may thus have interesting implications for bleb-based cell migration in both developmental and pathological contexts.

MATERIALS AND METHODS

Cell lines, growth conditions, and chemicals

HeLa (American Type Culture Collection [ATCC], CCL-2) and Cos7 (ATCC CRL-1651) cells were cultured in growth media composed of DMEM (Mediatech, Manassas, VA; #10-013-CV) containing 4.5 g/l L-glutamine, L-glucose, and sodium pyruvate, and supplemented with 10% fetal bovine serum (FBS; Sigma-Aldrich, St. Louis, MO; #F2442). HAP1 *myh9* (MIIA) KO and parental cells were purchased from Haplogen Genomics as previously described (Fenix *et al.*, 2016), and cultured in Iscove's minimal essential medium (IMDM) supplemented with 10% FBS. M2 melanoma cells were cultured in MEM supplemented with Earle's salts, 10 mM HEPES, and 10% FBS. Growth substrates were prepared by coating #1.5 glass coverslips (In Vitro Scientific; #D35-20-1.5N) with 10 µg/ml fibronectin (Corning, NY; #354008) in phosphate-buffered saline (Mediatech; #46-013-CM) at 37°C for 1 h.

For protein expression, cells were transiently transfected using Fugene 6 (Promega, Madison, WI; #E2691) as per the manufacturer's instructions overnight in a 24-well tissue culture plate (Corning) before plating on a growth substrate.

Alexa Fluor 488–goat anti-rabbit (#A11034) and Alexa Fluor 568–goat anti-rabbit (#A11036) were purchased from Thermo Fisher Scientific (Waltham, MA). Rabbit anti-myosin IIA (#909801) was purchased from BioLegends (San Diego, CA). Rabbit anti-myosin IIB (#8824S) and myosin IIC (#8189) were purchased from Cell Signaling Technology (Danvers, MA). Mouse anti-tubulin (#T6199) was purchased from Millipore Sigma (Darmstadt, Germany).

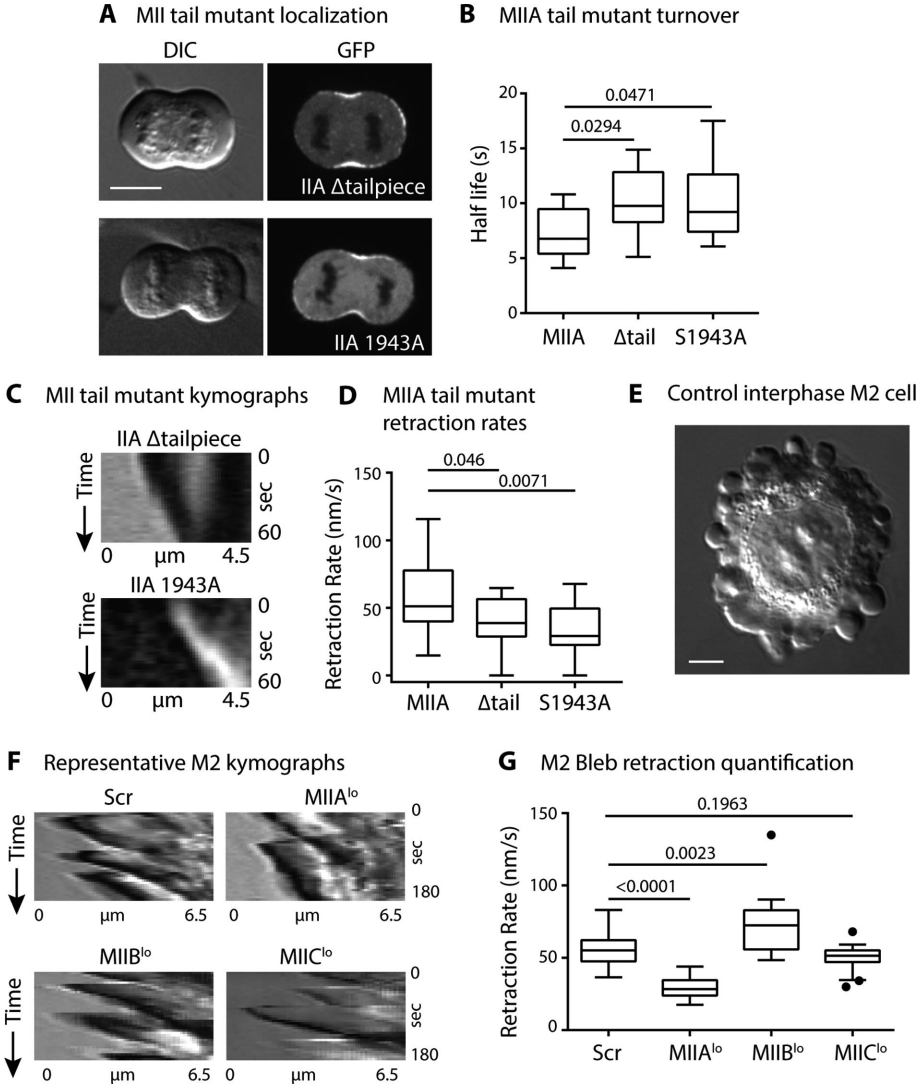

FIGURE 5: Phosphorylation of the nonhelical tailpiece regulates turnover at the cortex. (A) Representative DIC and fluorescence images showing localization of MII mutants in HAP1 KO cells. (B) Tukey plots comparing time for half-maximal recovery for MIIA tail mutants. $n = 10$ MIIA Δtailpiece and 12 MIIA S1943A expressing cells over three independent experiments. The MIIA FRAP data set is the same as Figure 3C and is shown only for comparison. (C) Representative kymographs for MIIA Δtailpiece and MIIA S1943A following cortex ablation in HAP1 KO cells. (D) Tukey plots comparing bleb retraction rates in HAP1 KO cells for MIIA tail mutants. $n = 17$ MIIA Δtailpiece and 15 MIIA S1943A expressing cells over three independent experiments. The MIIA data set is the same as in Figure 2C and is shown only for comparison. (E) DIC image of Scr control M2 cell 5 h postplating. (F) Representative kymographs for bleb retraction in Scr vs. MIIA^{lo}, MIIB^{lo}, and MIIC^{lo} M2 cells during interphase. (G) Tukey plots comparing bleb retraction rates for Scr vs. MIIA^{lo}, MIIB^{lo}, and MIIC^{lo} M2 cells. Scale bars in A and E: 10 and 5 μm, respectively. Exact p values stated over respective bars. Solid circles represent outliers.

Plasmids

MIIA mApple (Addgene; #54929) and MIIB mEmerald (Addgene; #54192) were gifts from Michael Davidson (National High Magnetic Field Laboratory). MIIA mEGFP (Addgene, Cambridge, MA; #11347) was a gift from Robert Adelstein (National Institutes of Health). MIIB mEGFP (Addgene; #35691) was a gift from Venkaiah Betapudi (Case Western Reserve University). MIIA Δtail (Addgene; #35689) was a gift from Thomas Egelhoff (Case Western Reserve University). The mEGFP tagged MIIB/A and MIIA/B chimeras were generously provided by Miguel Vincente-Manzanares (Universidad Autonoma de Madrid, Spain). MIIA S1943A and MIIB Δtail were created by mutagenizing MIIA mEGFP and MIIB mEmerald, respectively, using a site-directed PCR mutagenesis protocol as described previously (Liu and Naismith, 2008). The A/B/A chimera was created using Gibson Assembly. The fragments corresponding to the rod region of MIIB and corresponding to the motor and nonhelical tailpiece of MIIA were amplified using PCR, following which they were PCR purified and assembled using the NEB HiFi Gibson Assembly Kit according to the instructions provided by the manufacturer.

Live imaging and FRAP

Live imaging and FRAP experiments were performed on a Nikon Eclipse Ti-E inverted microscope equipped with a Yokogawa CSU-X1 spinning-disk head, 1.4 NA 60× oil objective, Andor DU-897 EMCCD, and a dedicated 100-mW 405-diode ablation laser, generously provided by the Nikon Center of Excellence at Vanderbilt University. The instrument was controlled using Nikon Elements AR software. Bleaching was performed for 500 ms using a pixel dwell time of 500 μs and 15% laser power with the same 2.7 μm × 2.7 μm region of interest (ROI) for all FRAP experiments. Samples were maintained at 37°C with 5% CO_2 in a Tokai Hit Stage incubator.

To image endogenous MIIA in fixed HAP1 cells, single optical sections through the middle of the cell were acquired using the 60× objective using the same parameters for GFP as used in the ablation and FRAP experiments. To image M2 cells, we used a Nikon Eclipse Ti wide-field system equipped with a 1.45 NA 100× objective with a Tokai Hit heated stage.

Cortical ablation

Laser damage–induced ablation of the polar cortex was performed on a Nikon Eclipse Ti-E inverted microscope equipped with a Yokogawa CSU-X1 spinning-disk head, 1.4 NA 60× oil objective, an Andor DU-897 EMCCD, and a dedicated 100-mW 405-diode ablation laser, generously provided by the Nikon Center of Excellence at Vanderbilt University. A 1.4 μm × 1.4 μm ROI was used for all experiments. A differential interference contrast (DIC) and/or fluorescence image was acquired before ablation, followed by ablation using a miniscanner. A pixel dwell time of 500 μs, 50% laser power was used for a duration of 1 s, followed by acquiring DIC or fluorescence images at 2 s intervals.

Knockdown experiments

Smart Pool Accell siRNA against MIIA (myh9 gene, #E-007668, #1-CCGUUGACUCAGUAUAGUU, #2-UCCACAUCUUCUAUUAUCU,

#3-GUGUGGUCAUCAAUCCUUA, #4-CUUAUGAGCUCCAAGGAUG), MIIB (myh10 gene, #E-023017, #1-GGACUAAUCUAUACUUAUU, #2-UGUCAAUGCUUAAAGUAGU, #3-CGAGGAUCCAGAGAGGUAU, #4-CCAAUUUACUCUGAGAAUA), and MIIC (myh14 gene, #E027149, #1-CCAUGAACCGUGAAGUGAC, #2-CCCUCGUUAUUGAUCUAUA, #3-CUCUCACUCUCUACGUAGC, #4-CCCUUGAGUCUAAGUUGGC) were purchased from GE Dharmacon (Lafayette, CO). Knockdown experiments were performed in 24-well plates using Lipofectamine 2000 (Life Technologies; #1690146) as per instructions provided by the manufacturer. Knockdown was performed for 72 h, after which cells were either plated on the growth substrate for imaging or lysed for Western blot experiments.

Western blotting

Gel samples were prepared by mixing cell lysates with LDS sample buffer (Life Technologies; #NP0007) and sample reducing buffer (Life Technologies; #NP00009) and boiled at 95°C for 5 min. Samples were resolved on Bolt 4–12% gradient Bis-Tris gels (Life Technologies; #NW04120BOX). Protein bands were blotted onto a nylon membrane (Millipore). Blots were blocked using 5% dry milk (Research Products International, Mt. Prospect, IL; # M17200-100.0) in Tris buffered saline with 0.1% Tween-20 (TBST). Antibody incubations were also performed in 5% dry milk in TBST. Blots were developed using the Immobilon Chemiluminescence Kit (Millipore; #WBKLS0500).

Calibration of protein expression levels in HAP1 KO cells

For quantification of exogenous plasmid expression in the HAP1 knockout cell line, MIIA GFP was expressed in the KO cell line. Cells were fixed and stained with an antibody against the rod domain of MIIA in the red channel. In parallel, the untransfected parental HAP1 cell line was also fixed and stained for MIIA rod domains in the red channel. GFP expression in the cytoplasm was then calibrated against the corresponding intensity of endogenous MIIA in the cytoplasm. The intensity in the cytoplasm was also normalized against the relative enrichment at the polar cortex. Imaging all the GFP-tagged mutants with the exact same imaging parameters allowed us to compare expression levels across all mutants tested.

Data quantification

For quantification of bleb retraction rates, DIC time montages were acquired at 2 s intervals following cortex ablation. Images were first aligned using the StackReg plug-in in Fiji. A 3-pixel-thick line was drawn perpendicular to the cortex boundary as shown in Figure 1A to create a kymograph using the MultipleKymograph plug-in in Fiji. Retraction rates were calculated as the ratio of horizontal distance (distance) in nanometers to the vertical distance (time) in seconds (shown as white lines in the kymograph in Figure 1A).

For quantification of the timing of arrival in blebs as shown in Figure 1C, fluorescence montages acquired at 2 s intervals were used. Three time points were acquired before ablation. A 3-pixel-thick line was drawn perpendicular to the cortex boundary and saved in the ROI manager in ImageJ. The same line was then used to create kymographs for both MIIA and MIIB channels. A 15-pixel-thick segmented line was then drawn along the retracting cortex boundary starting at the first time point (6 s before ablation) until the end of bleb retraction. The intensities were then normalized to the maximum fluorescence for the corresponding channel during bleb retraction. Recruitment dynamics were then compared for the first 60 s.

For quantification of FRAP data, confocal time montages acquired at 2 s intervals were first aligned using the StackReg plug-in in Fiji, followed by drawing ROIs around the bleached region, an unbleached region, and background. Mean intensity over time was calculated for each of the three ROIs using the multimeasure function in the ROI manager. Subsequent analysis was performed using the EasyFRAP algorithm in MATLAB as previously described (Rapsomanski *et al.*, 2015). Briefly, a double normalization was performed to account for background correction and photobleaching, followed by fitting the normalized curves to a second-degree exponential to obtain the half-maximal recovery time and mobile fraction (see Rapsomanski *et al.*, 2015, for details on fitting equations and normalization). Curves with poor fits (with $R^2 < 0.9$) were not included for analysis. We noted negligible bleaching (<5% for GFP). FRAP curves averaged using entire data sets for display (Figures 3–5) were generated in Excel.

Statistics

Statistical significance was determined using Mann–Whitney's *U* test using GraphPad Prism. All graphs are represented as Tukey plots showing boxes (with median, Q1, Q3 percentiles), whiskers (minimum and maximum values within 1.5 times interquartile range), and outliers (solid circles). No outliers were removed from the analysis.

ACKNOWLEDGMENTS

We thank Matthew Tyska for the gift of M2 melanoma cells, Miguel Vincente-Manzanares for providing the MII chimeras, and Karren Hyde, Meredith Weck, and MariaSanta Mangione for valuable feedback and advice. We thank the Nikon Center of Excellence, Vanderbilt University, for providing access to the Nikon spinning-disk microscope and technical support. The raw data generated in the current study are available from the corresponding author upon reasonable request. This work was funded by a Maximizing Investigators' Research Award (MIRA) from the National Institute of General Medical Sciences (R35 GM125028) awarded to D.T.B. and an American Heart Association Predoctoral Fellowship (18PRE33960551) to N.T.

REFERENCES

Beach JR, Bruun KS, Shao L, Li D, Swider Z, Remmert K, Zhang Y, Conti MA, Adelstein RS, Rusan NM, *et al.* (2017). Actin dynamics and competition for myosin monomer govern the sequential amplification of myosin filaments. Nat Cell Biol 19, 85–93.

Bergert M, Erzberger A, Desai RA, Aspalter IM, Oates AC, Charras G, Salbreux G, Paluch EK (2015). Force transmission during adhesion-independent migration. Nat Cell Biol 17, 524–529.

Blaser H, Reichman-Fried M, Castanon I, Dumstrei K, Marlow FL, Kawakami K, Solnica-Krezel L, Heisenberg C-P, Raz E (2006). Migration of zebrafish primordial germ cells: a role for myosin contraction and cytoplasmic flow. Dev Cell 11, 613–627.

Bluteau D, Glembotsky AC, Raimbault A, Balayn N, Gilles L, Rameau P, Nurden P, Alessi MC, Debili N, Vainchenker W, *et al.* (2012). Dysmegakaryopoiesis of FPD/AML pedigrees with constitutional RUNX1 mutations is linked to myosin II deregulated expression. Blood 120, 2708–2718.

Bovellan M, Romeo Y, Biro M, Boden A, Chugh P, Yonis A, Vaghela M, Fritzsche M, Moulding D, Thorogate R, *et al.* (2014). Cellular control of cortical actin nucleation. Curr Biol 24, 1628–1635.

Breckenridge MT, Dulyaninova NG, Egelhoff TT, Wang Y-L (2008). Multiple regulatory steps control mammalian nonmuscle myosin II assembly in live cells. Mol Biol Cell 20, 338–347.

Brown ME, Bridgman PC (2003). Retrograde flow rate is increased in growth cones from myosin IIB knockout mice. J Cell Sci 116, 1087–1094.

Charras GT, Coughlin M, Mitchison TJ, Mahadevan L (2008). Life and times of a cellular bleb. Biophys J 94, 1836–1853.

Charras GT, Hu C-K, Coughlin M, Mitchison TJ (2006). Reassembly of contractile actin cortex in cell blebs. J Cell Biol 175, 477–490.
Derycke L, Stove C, Vercoutter-Edouart A-S, De Wever O, Dollé L, Colpaert N, Depypere H, Michalski J-C, Bracke M (2011). The role of non-muscle myosin IIA in aggregation and invasion of human MCF-7 breast cancer cells. Int J Dev Biol 55, 835–840.
Dulyaninova NG, Bresnick AR (2013). The heavy chain has its day: regulation of myosin-II assembly. Bioarchitecture 3, 77–85.
Dulyaninova NG, House RP, Betapudi V, Bresnick AR, Wang Y (2007). Myosin-IIA heavy-chain phosphorylation regulates the motility of MDA-MB-231 carcinoma cells. Mol Biol Cell 18, 3144–3155.
Dulyaninova NG, Malashkevich VN, Almo SC, Bresnick AR (2005). Regulation of myosin-IIA assembly and Mts1 binding by heavy chain phosphorylation. Biochemistry 44, 6867–6876.
Even-Ram S, Doyle AD, Conti MA, Matsumoto K, Adelstein RS, Yamada KM (2007). Myosin IIA regulates cell motility and actomyosin–microtubule crosstalk. Nat Cell Biol 9, 299–309.
Fenix AM, Taneja N, Buttler CA, Lewis J, Van Engelenburg SB, Ohi R, Burnette DT (2016). Expansion and concatenation of non-muscle myosin IIA filaments drive cellular contractile system formation during interphase and mitosis. Mol Biol Cell 27, 1465–1478.
Friedl P, Wolf K (2003). Tumour-cell invasion and migration: diversity and escape mechanisms. Nat Rev Cancer 3, 362–374.
Fritzsche M, Erlenkämper C, Moeendarbary E, Charras G, Kruse K (2016). Actin kinetics shapes cortical network structure and mechanics. Sci Adv 2, e1501337.
Fritzsche M, Lewalle A, Duke T, Kruse K, Charras G, Mogilner A (2013). Analysis of turnover dynamics of the submembranous actin cortex. Mol Biol Cell 24, 757–767.
Goudarzi M, Banisch TU, Mobin MB, Maghelli N, Tarbashevich K, Strate I, van den Berg J, Blaser H, Bandemer S, Paluch E, *et al.* (2012). Identification and regulation of a molecular module for bleb-based cell motility. Dev Cell 23, 210–218.
Hu A, Wang F, Sellers JR (2002). Mutations in human nonmuscle myosin IIA found in patients with May-Hegglin anomaly and Fechtner syndrome result in impaired enzymatic function. J Biol Chem 277, 46512–46517.
Jiao M, Wu D, Wei Q (2018). Myosin II–interacting guanine nucleotide exchange factor promotes bleb retraction via stimulating cortex reassembly at the bleb membrane. Mol Biol Cell 29, 643–656.
Kageyama T (1977). Motility and locomotion of embryonic cells of the medaka, *Oryziaslatipes*, during early development. Dev Growth Differ 19, 103–110.
Kelley CA, Adelstein RS (1990). The 204-kDa smooth muscle myosin heavy chain is phosphorylated in intact cells by casein kinase II on a serine near the carboxyl terminus. J Biol Chem 265, 17876–17882.
Kovács M, Wang F, Hu A, Zhang Y, Sellers JR (2003). Functional divergence of human cytoplasmic myosin II: kinetic characterization of the non-muscle IIA isoform. J Biol Chem 278, 38132–38140.
Liu H, Naismith JH (2008). An efficient one-step site-directed deletion, insertion, single and multiple-site plasmid mutagenesis protocol. BMC Biotechnol 8, 91.
Lordier L, Jalil A, Aurade F, Larbret F, Larghero J, Debili N, Vainchenker W, Chang Y (2008). Megakaryocyte endomitosis is a failure of late cytokinesis related to defects in the contractile ring and Rho/Rock signaling. Blood 112, 3164–3174.
Maeda J, Hirano T, Ogiwara A, Akimoto S, Kawakami T, Fukui Y, Oka T, Gong Y, Guo R, Inada H, *et al.* (2008). Proteomic analysis of stage I primary lung adenocarcinoma aimed at individualisation of postoperative therapy. Br J Cancer 98, 596–603.
Rapsomanski MA, Cinquemani E, Giakoumakis NN, Kotsantis P, Lygeros J, Lygerou Z (2015). Inference of protein kinetics by stochastic modeling and simulation of fluorescence recovery after photobleaching experiments. Bioinformatics 31, 355–362.
Sahai E, Marshall CJ (2003). Differing modes of tumour cell invasion have distinct requirements for Rho/ROCK signalling and extracellular proteolysis. Nat Cell Biol 5, 711–719.
Salbreux G, Charras G, Paluch E (2012). Actin cortex mechanics and cellular morphogenesis. Trends Cell Biol 22, 536–545.
Sedzinski J, Biro M, Oswald A, Tinevez J-Y, Salbreux G, Paluch E (2011). Polar actomyosin contractility destabilizes the position of the cytokinetic furrow. Nature 476, 462–466.
Sezgin E, Levental I, Mayor S, Eggeling C (2017). The mystery of membrane organization: composition, regulation and roles of lipid rafts. Nat Rev Mol Cell Biol 18, 361.
Smutny M, Cox HL, Leerberg JM, Kovacs EM, Conti MA, Ferguson C, Hamilton NA, Parton RG, Adelstein RS, Yap AS (2010). Myosin II isoforms identify distinct functional modules that support integrity of the epithelial zonula adherens. Nat Cell Biol 12, 696–702.
Tinevez J-Y, Schulze U, Salbreux G, Roensch J, Joanny J-F, Paluch E (2009). Role of cortical tension in bleb growth. Proc Natl Acad Sci USA 106, 18581–18586.
Trinkaus JP (1973). Surface activity and locomotion of *Fundulus* deep cells during blastula and gastrula stages. Dev Biol 30, 68–103.
Vicente-Manzanares M, Koach MA, Whitmore L, Lamers ML, Horwitz AF (2008). Segregation and activation of myosin IIB creates a rear in migrating cells. J Cell Biol 183, 543–554.
Vicente-Manzanares M, Ma X, Adelstein RS, Horwitz AR (2009). Non-muscle myosin II takes centre stage in cell adhesion and migration. Nat Rev Mol Cell Biol 10, 778.
Wang F, Kovacs M, Hu A, Limouze J, Harvey EV, Sellers JR (2003). Kinetic mechanism of non-muscle myosin IIB: functional adaptations for tension generation and maintenance. J Biol Chem 278, 27439–27448.